Progress In Electromagnetics Research Letters, Vol. 118, 41-46, 2024
PIER Letters

(Received 8 January 2024, Accepted 28 February 2024, Scheduled 4 March 2024)

Design of Dual-Band FPD with High Selectivity

Tian Tian Zhang*, Lei Chen, Meng Liu, Jin Yi Liu, and Min Wang

School of Electronic and Information Engineering, Xi'an Technological University, Xi'an 710021, China

ABSTRACT: In this brief, a dual-band filtering power divider (FPD) with high selectivity and independently controllable passbands is designed. The proposed FPD consists of asymmetric folded F-type resonators (AFFRs) and quarter-wavelength three parallel-coupled lines (TPCLs). The center frequencies of the dual bands can be determined by adjusting the physical lengths of AFFRs. Meanwhile, TPCLs can increase the transmission paths and introduce multiple transmission zeros (TZs) to achieve high selectivity. For demonstration, the proposed FPD is designed, fabricated, and measured. The center frequencies are 2.59/3.63 GHz with the 3-dB fractional bandwidths (FBWs) of 12.95% and 7.88%, and the isolation between port 2 and port 3 is better than 12.56/21.03 dB. The minimum insertion losses are better than 0.54/0.32 dB in each passband. The simulated results are compared with measured ones, and good agreement is realized.

1. INTRODUCTION

Filters and power dividers are widely applied in microwave wireless communication systems. In order to achieve multifunction and miniaturization, filters and power dividers are integrated. T Filtering power divider (FPD) not only realizes the frequency selection, but also achieves signals division. In [1], a dual-band FPD was proposed by using three parallel-coupled lines (TPCLs), transmission lines, and a pair of short-ended parallel coupled lines. Unfortunately, only three transmission zeros (TZs) are generated, and the selectivity of passbands can be further enhanced. In [2–4], filters and FPD were composed of TPCLs, and multiple transmission zeros (TZs) have been generated, due to the horizontal transmission interference of the resonator and the new coupling path. In [5–9], two pairs of dual-resonance resonators (DRRs), two in-parallel transmission lines or short-ended stepped-impedance resonators (SESIRs) were employed to design dual-band FPDs. Three TZs were generated by employing mixed electric and magnetic couplings, so two passbands selectivity was enhanced. In [10–12], Kron-Branin modeling and two-stage passive NGD cells have been proposed, providing new ideas for the diversity of modeling. In [13], a novel port-to-port isolation was proposed to design an FPD with good isolation, and the minimum insertion loss can be enhanced further. However, two TZs were realized by multiple-mode resonators, and the size of FPD has been increased.

In this brief, a dual-band FPD based on asymmetric folded F-type resonators (AFFRs) is investigated. The two output ports are connected in parallel by a quarter-wavelength transmission line and the shunt connection through one resistor, aiming to realize high isolation between output ports. Meanwhile, the half-wavelength resonator is used to realize the passband working at 2.56 GHz and an open-stub loaded at the middle position working at 3.61 GHz. The two center frequencies and fractional bandwidths (FBWs) of the dual bands can be controlled independently by changing the parameters of AFFRs and the coupling gaps between TPCLs and AFFRs, respectively. The traditional method to improve FPD selectivity is employing more transmission paths. However, the size of the designed FPD will increase. In this brief, interdigital coupling lines are used to introduce extra transmission paths while keeping the FPD size unchanged. The simulated and measured results are in good agreement.

2. DUAL-BAND FPD

2.1. Asymmetric Short Stub-Loaded Resonator

The traditional center stub-loaded resonator (CSLR) consists of a half-wavelength uniform impedance resonator (UIR) and an open-stub loaded at the middle position shown in Fig. 1(a), where Y_1, Y_2, L_{r1}, and L_{r2} denote the characteristic admittances, length of the open-stub, and the folded resonator, respectively. The even-odd mode equivalent circuits are shown in Figs. 1(b) and (c). In order to simplify the calculation, $Y_2 = 2Y_1$ is set, and the input impedances $Z_{in,odd}$ and $Z_{in,even}$ can be expressed as [14]:

$$Z_{in,odd} = -\frac{\tan(\theta_1)}{jY_1} \tag{1}$$

$$Z_{in,even} = \frac{2Y_1 - Y_2\tan(\theta_1)\tan(\theta_2)}{jY_1\left(Y_1\tan(\theta_1) + Y_2\tan(\theta_2)\right)} \tag{2}$$

Therefore, the even-odd mode resonant frequencies are calculated as:

$$f_1 = f_{odd} = \frac{c}{2L_{r2}\sqrt{\varepsilon_{eff}}} \tag{3}$$

$$f_2 = f_{even} = \frac{c}{\left(L_{r2} + 2L_{r1}\right)\sqrt{\varepsilon_{eff}}} \tag{4}$$

where c expresses the light speed in free space, and ε_{eff} is the effective dielectric constant of the substrate. Based on formu-

* Corresponding author: Tiantian Zhang (ztt162460@163.com).

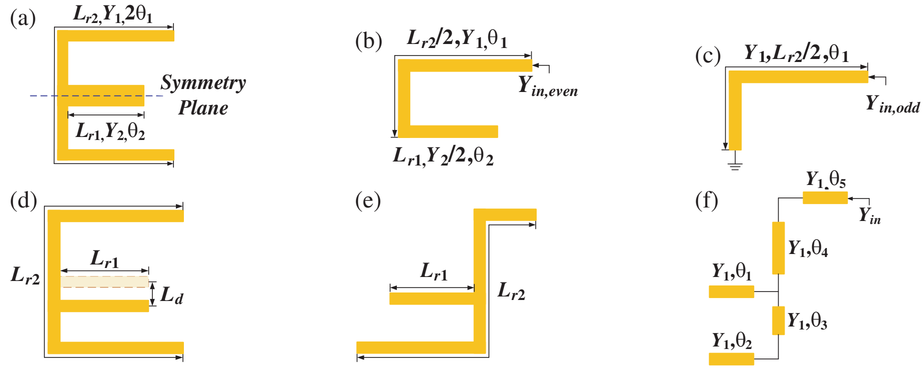

FIGURE 1. (a) CSLR, (b) even-mode and (c) odd-mode equivalent circuit of CSLR, (d) asymmetric short stub-loaded resonator, (e) AFFR and (f) equivalent circuit of AFFR.

las (3) and (4), the even-mode determines the higher resonant frequency, and the odd-mode defines the lower one.

In Fig. 1(d), L_d is the displacement of the loaded resonator relative to the center open-stub. CSLR is folded to realize miniaturization, as shown in Fig. 1(e). The AFFR introduces an additional resonance mode because the position of open-loaded stub is unlimited. In order to simplify the calculation, the same characteristic impedance of AFFR is designed and used for analysis. The equivalent circuit of AFFR is given in Fig. 1(f), where θ_T ($\theta_T = \theta_2+\theta_3+\theta_4+\theta_5$) is the electrical length of UIR; the electrical length of the loaded stub is θ_1; and $\theta_2+\theta_3 \neq \theta_4+\theta_5$. α and β are defined as follows:

$$\alpha = \frac{\theta_2+\theta_3}{\theta_2+\theta_3+\theta_4+\theta_5} = \frac{\theta_2+\theta_3}{\theta_T} \tag{5}$$

$$\beta\frac{\theta_1}{\theta_2+\theta_3+\theta_4+\theta_5} = \frac{\theta_1}{\theta_T} \tag{6}$$

where α is the ratio of the shorter section to total length of UIR, and β is defined as the radio of the loaded stub to the total length of UIR.

2.2. Dual-Band FPD Design

Figure 2(a) illustrates the configuration of the proposed dual-band FPD, which consists of AFFRs, TCLRs, and an isolation resistor. The transmission-line equivalent circuit is shown in Fig. 2(b). For even-odd mode excitation, the equivalent circuits are given in Figs. 2(c) and (d), where θ_i ($i = 1, 2, 3$) represents the electrical length, and Z_i ($i = 1, 2, 3$) is the impedance of the microstrip line.

The end-coupling and TPCL are exhibited in Figs. 3(a) and (b). TPCL is composed of interdigital coupling lines, which increases the transmission paths and achieves two TZs. Meanwhile, the out-of-band characteristics are improved without influencing the in-band characteristics. The novel TPCL generates TZ_2 and TZ_3 to enhance the selectivity in Fig. 3(c). It can be obtained that the out-of-band suppression is controlled by the different lengths of L_1 (total length of the interdigital coupled line), as shown in Fig. 3(d).

For dual bands, the half-wavelength resonator realizes the lower frequency band (f_1, 2.59 GHz), and f_1 is controlled by L_{r2} while the higher frequency band (f_2, 3.63 GHz) is achieved by employing L_{r2} and L_5. In order to explain the effects of AFFR lengths on two center frequencies, simulation calculations are performed on each branch, and the results are shown in Fig. 4. As shown in Figs. 4(a) to (d), f_1 and f_2 decrease with the increase of $L_r = L_4+L_6$, L_3, L_7, L_8. f_2 can be controlled independently by $L_5(L_{r1} = L_5)$ as shown in Fig. 5. Based on formula (3), the lower resonant frequency f_{odd} for f_1 is affected by the value of $L_{r2}(L_r + L_3 + L_7)$. Similarly, f_{even} for f_2 is influenced by the dimensions of the open-stub loaded.

The FBWs are controlled by the coupling gaps S_1 and S_3, because AFFRs are fed by TPCL. FBW_1 (fractional bandwidth of the first passband, the same as below) is determined independently by physical length S_1, as shown in Fig. 6(a). Meanwhile, FBW_1 and FBW_2 vary with the coupling gap S_3, and quasi-independent control of FBW_1 and FBW_2 can be realized by S_1 and S_3.

Due to the symmetrical structure of the proposed dual-band FPD, to simplify the calculation, the three-port circuit can be simplified as its half-two-port bisection network for isolation analysis [13]. As given in Figs. 2(c) and (d), S_{22} and S_{23} are defined as

$$S_{22} = \frac{\Gamma_e+\Gamma_o}{2} \tag{7}$$

$$S_{32} = \frac{\Gamma_e-\Gamma_o}{2} \tag{8}$$

where Γ_e and Γ_o are the reflection coefficients of the even-odd mode circuit at port 2. Γ_e and Γ_o can be given by

$$\Gamma_e = \frac{Z_{ine}-Z_0}{Z_{ine}+Z_0} \tag{9}$$

$$\Gamma_o = \frac{Z_{ino}-Z_0}{Z_{ino}+Z_0} \tag{10}$$

where Z_0 is the impedance of port. Z_{ine} is the input impedance of the even-mode circuit and can be calculated as

$$Z_{ine} = Z_4\frac{Z_{ine}^1 + jZ_4\tan\theta_{10}}{Z_4 + jZ_{ine}^1\tan\theta_{10}} \tag{11}$$

where

$$Z_{ine}^1 = -jZ_{a3}\cot\theta_{10} + \frac{Z_{b3}^2\csc^2\theta_{10}}{Z_{ine}^2 - jZ_{a3}\cot\theta_{10}} \tag{12}$$

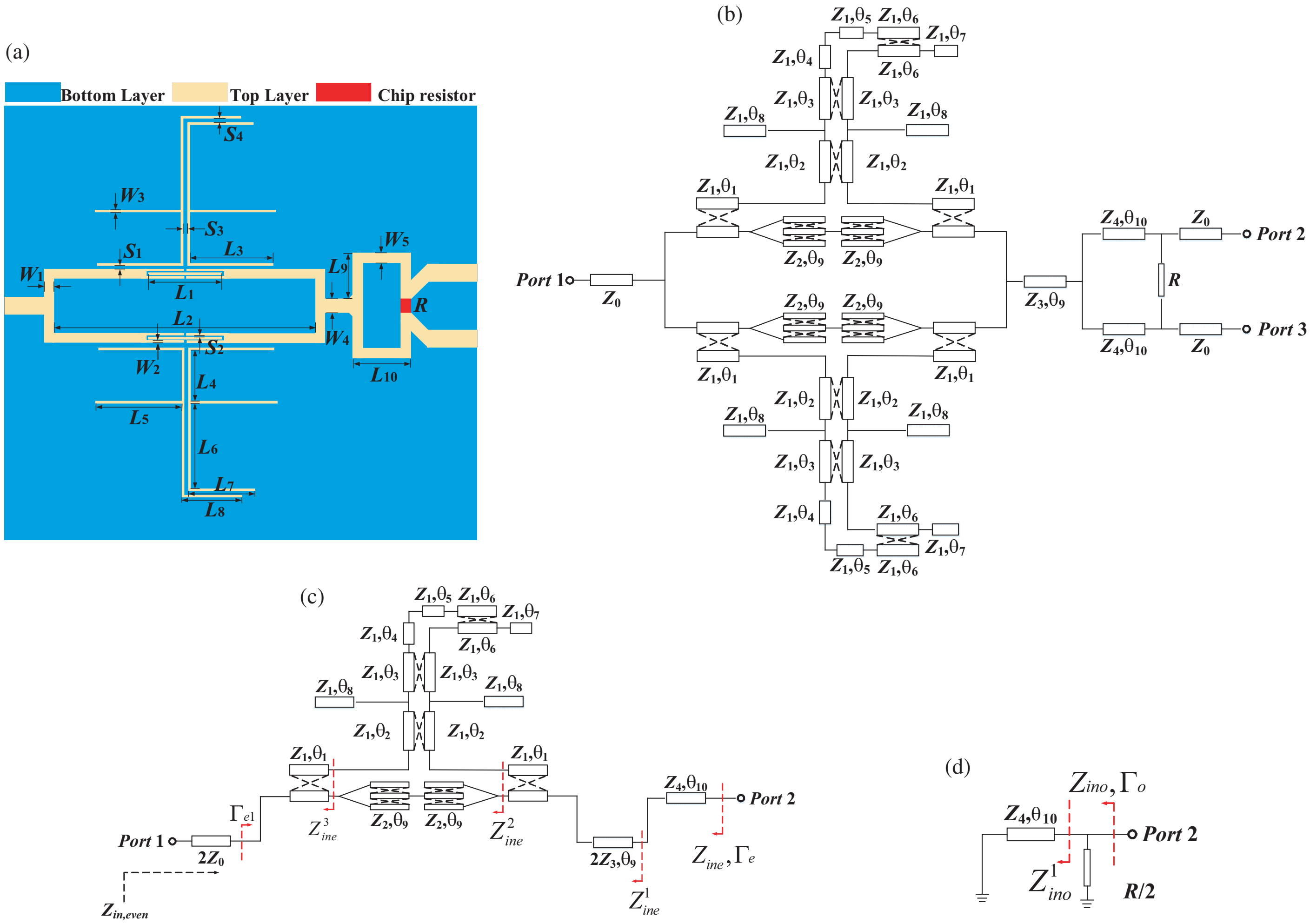

FIGURE 2. (a) Topology of the proposed dual-band FPD, (b) transmission-line equivalent circuit, (c) even-mode and (d) odd-mode equivalent circuit of the proposed FPD.

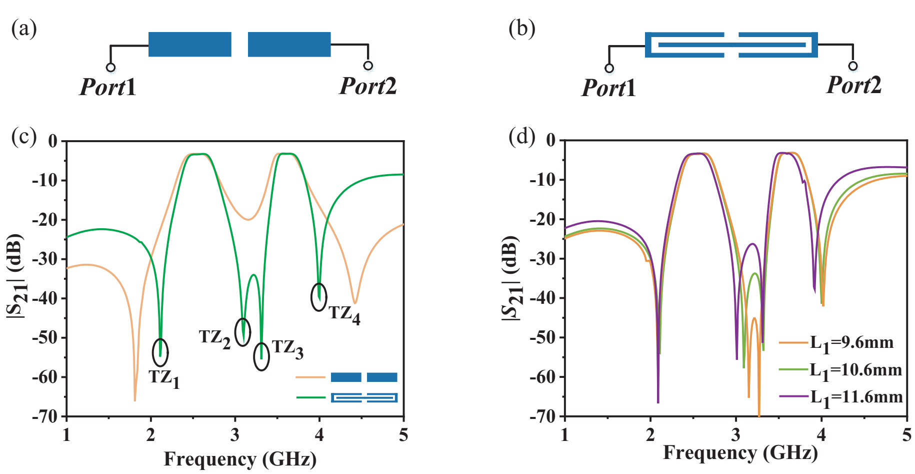

FIGURE 3. (a) End-coupling, (b) TPCL, comparison of selectivity with (c) different types of coupling and (d) sizes of the interdigital coupled line.

$$Z_{ine}^{2} = \frac{jZ_1 Z_{ine}^{3} \cot\left(\sum\limits_{i=2}^{8} \theta i\right)}{jZ_1 \cot\left(\sum\limits_{i=2}^{8} \theta i\right) - Z_{ine}^{3}} \tag{13}$$

$$Z_{ine}^{3} = -jZ_{a1} \cot\theta_{10} + \frac{Z_{b1}^{2} \csc^{2}\theta_{10}}{2Z_0 - jZ_{a1}\cot\theta_{10}} \tag{14}$$

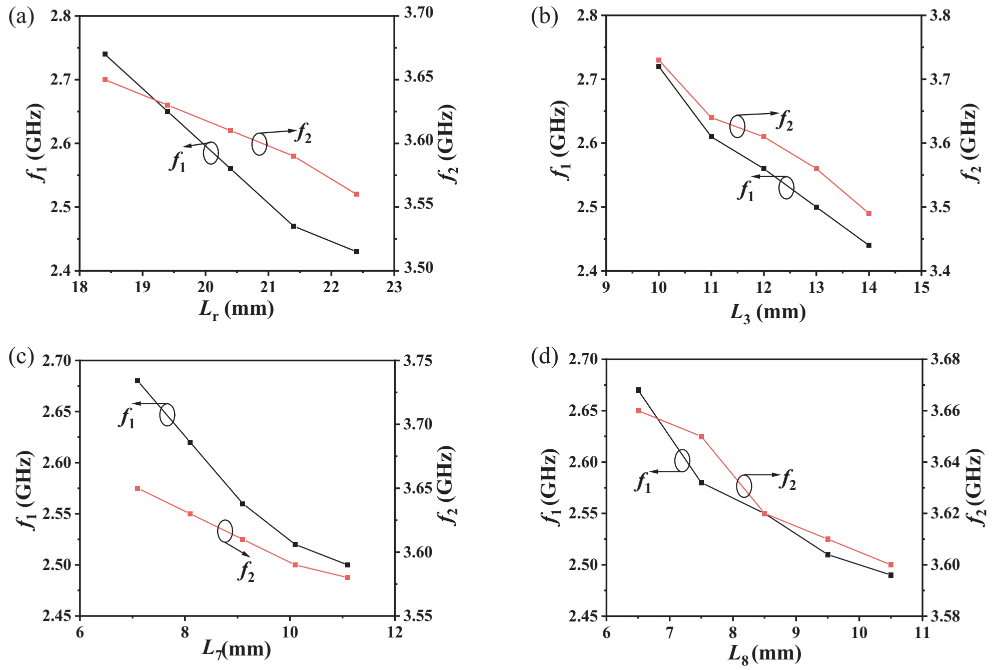

FIGURE 4. Variation of odd-mode resonance frequency of AFFR with parameters (a) L_r, (b) L_3, (c) L_7 and (d) L_8.

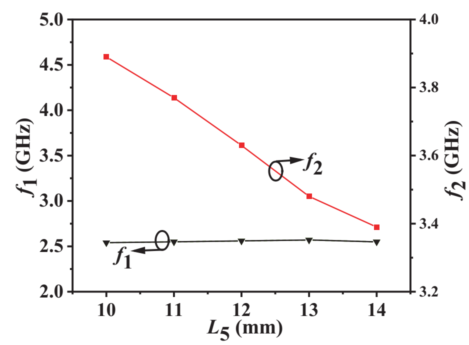

FIGURE 5. Variation of even-mode resonance frequency of AFFR with different L_5.

$$\begin{cases} Z_{ai} = \dfrac{Z_{ei} + Z_{oi}}{2} \\ Z_{bi} = \dfrac{Z_{ei} - Z_{oi}}{2} \end{cases} \quad (i = 1 \quad or \quad 3) \tag{15}$$

The input impedance Z_{ino} can be expressed as

$$Z_{ino} = \frac{Z_{ino}^1 R}{R + 2Z_{ino}^1} \tag{16}$$

where

$$Z_{ine}^1 = jZ_4 \tan\theta_{10} \tag{17}$$

When $f_0 = (f_1 + f_2)/2$, $\theta = 90°$ is defined. f_1 and f_2 are the center frequencies of the two passbands of the proposed FPD. $S_{22} = 0$, and $S_{32} = 0$, (11) and (16) can be derived as

$$Z_{ine} = Z_0 = \frac{Z_4^2 Z_{b1}^2}{2Z0 Z_{b3}^2} \tag{18}$$

$$Z_{ino} = Z_0 = \frac{R}{2} \tag{19}$$

If $Z_{b1} = Z_{b3}$, one can obtain that $Z_4 = \sqrt{2}Z_0$ and $R = 2Z_0$. The in-band isolation increases from 5.01/5.93 dB to 12.56/21.03 dB in Fig. 7, respectively.

3. SIMULATION AND MEASUREMENT RESULTS

In this brief, the proposed dual-band FPD is designed on an F4BM-2 substrate with a thickness of 0.8 mm and a dielectric constant of 2.2. The measurement of FPD is done by an Agilent Network Analyzer N5230A.

In Fig. 2(a), the cases of the dual-band FPD are: $L_1 = 10.6$ mm, $L_2 = 37.46$ mm, $L_3 = 12$ mm, $L_4 = 7.3$ mm, $L_5 = 12.3$ mm, $L_6 = 12.2$ mm, $L_7 = 9.4$ mm, $L_8 = 8.5$ mm, $L_9 = 6.5$ mm, $L_{10} = 8.2$ mm, $W_1 = 1.24$ mm, $W_2 = 0.3$ mm, $W_3 = 0.3$ mm, $W_4 = 2$ mm, $W_5 = 1.36$ mm, $S_1 = 0.1$ mm, $S_2 = 0.17$ mm, $S_3 = 0.6$ mm, $S_4 = 0.6$ mm, $R = 100\,\Omega$. Fig. 8(a) shows the fabricated dual-band FPD, and its overall size is 67.38 mm $\times$ 61.96 mm ($0.79\lambda_g \times 0.73\lambda_g$, where λ_g is the guide wavelength at 2.59 GHz). In Fig. 8(a), the

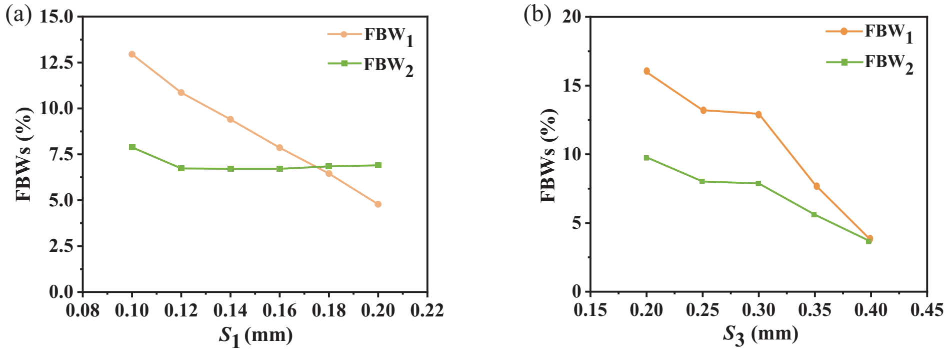

FIGURE 6. Variation of the two center frequencies with the parameters (a) S_1 and (b) S_3.

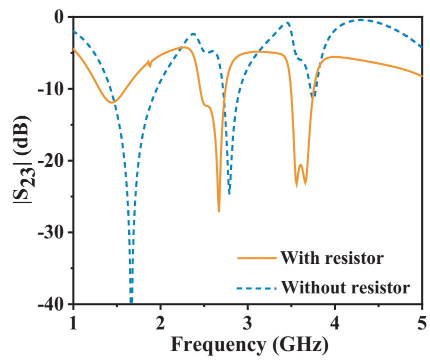

FIGURE 7. Effect of resistor on isolation.

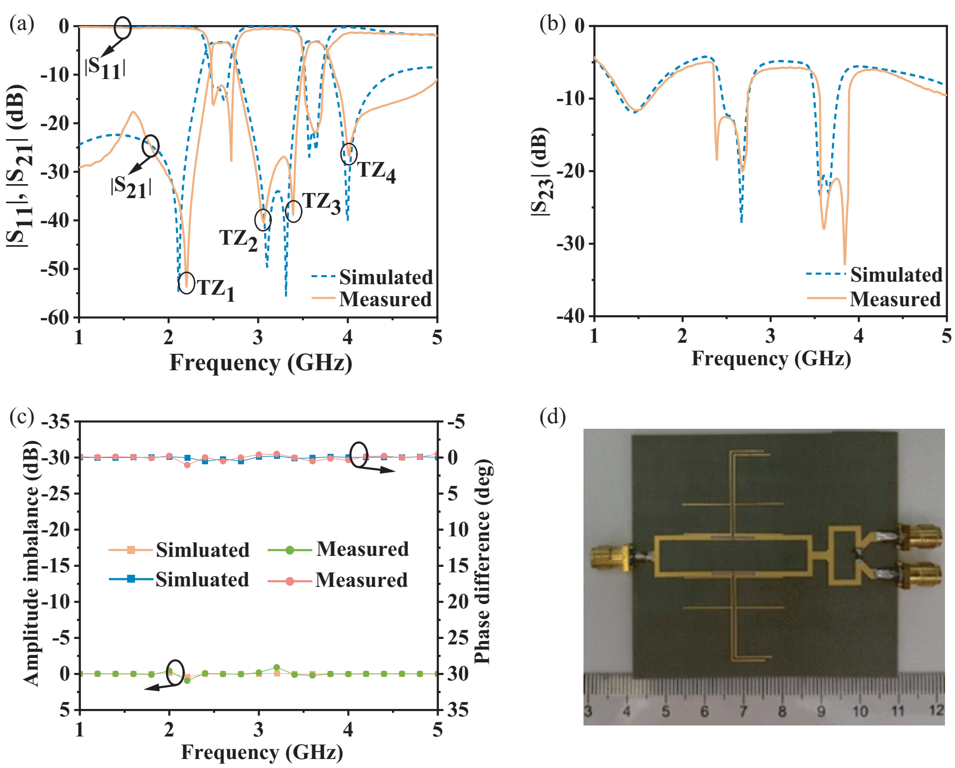

FIGURE 8. Simulated and measured results of the proposed dual-band FPD (a) $|S_{11}|$ and $|S_{21}|$, (b) $|S_{23}|$, (c) amplitude imbalance and phase difference, and (d) photograph of the proposed FPD.

TABLE 1. Comparisons with some reported dual-band FPDs.

Ref.	f_0 (GHz)	IL (dB)	3-dB FBW (%)	Number of TZs	Isolation	Size ($\lambda g \times \lambda g$)
[1]	2.4/3.8	N/A	43.6/25.1	3	> 15.0	0.49×0.49
[6]	4.11/6.56	0.8/1.8	N/A	0	17/26	0.133×0.133
[7]	2.46/5.19	1.74/2.12	4.5/2.3	3	15.3/22.5	0.09×0.09
[9]	5.5/8.3	0.9/1.5	N/A	0	> 20	2.15×0.89
This work	**2.59/3.63**	**0.54/0.32**	**12.95/7.88**	**4**	**12.56/21.03**	$\mathbf{0.79 \times 0.73}$

FBW: fractional bandwidth. IL: insertion loss. TZs: transmission zeros.

measured two center frequencies are 2.59/3.63 GHz with 3-dB FBWs of 12.95/7.88%. The insertion losses in-band are less than 0.54/0.32 dB (excluding 3-dB power division), and the return losses are better than 12.8/21.8 dB. The isolation is better than 12.56 dB in Fig. 8(b). In addition, four TZs (2.11, 3.1, 3.31, and 4 GHz) are realized successfully at the edges of the passbands to achieve higher selectivity. The phase difference and magnitude imbalance within the passbands are less than 1° and 0.5 dB, respectively in Fig. 8(c). Table 1 summarizes the comparisons in the key performance parameters between the proposed FPD and other reported ones. The proposed one is featured by the low insertion losses and high selectivity.

4. CONCLUSION

In this letter, a dual-band FPD with good performance has been proposed. The physical size of AFFRs can independently control the center frequencies of the two passbands, and the 3-dB FBWs can be determined by the coupling gaps between AFFRs and TPCLs. The TPCLs can increase the transmission paths and introduce two TZs to effectively improve the selectivity. Due to the small insertion loss and good selectivity, the proposed dual-band FPD is widely used in the application of wireless communication systems.

REFERENCES

[1] Luo, Z., G. Zhang, H. Wang, N. Li, K. W. Tam, L. Tang, W. Tang, and J. Yang, "Dual-band and triple-band filtering power dividers using coupled lines," *IEEE Transactions on Circuits and Systems II: Express Briefs*, Vol. 70, No. 4, 1440–1444, Apr. 2023.

[2] Wei, F., H. J. Yue, X. H. Zhang, and X.-W. Shi, "A balanced quad-band bpf with independently controllable frequencies and high selectivity," *IEEE Access*, Vol. 7, 110 316–110 322, Jul. 2019.

[3] Wei, F., C. Y. Zhang, C. Zeng, and X. W. Shi, "A reconfigurable balanced dual-band bandpass filter with constant absolute bandwidth and high selectivity," *IEEE Transactions on Microwave Theory and Techniques*, Vol. 69, No. 9, 4029–4040, Sep. 2021.

[4] Zhao, X.-B., F. Wei, P. F. Zhang, and X. W. Shi, "Mixed-mode magic-ts and their applications on the designs of dual-band balanced out-of-phase filtering power dividers," *IEEE Transactions on Microwave Theory and Techniques*, Vol. 71, No. 9, 3896–3905, Sep. 2023.

[5] Wen, P., Z. Ma, H. Liu, S. Zhu, B. Ren, Y. Song, X. Wang, and M. Ohira, "Dual-band filtering power divider using dual-resonance resonators with ultrawide stopband and good isolation," *IEEE Microwave and Wireless Components Letters*, Vol. 29, No. 2, 101–103, Feb. 2019.

[6] Sajadi, A., A. Sheikhi, and A. Abdipour, "Analysis, simulation, and implementation of dual-band filtering power divider based on terminated coupled lines," *IEEE Transactions on Circuits and Systems II: Express Briefs*, Vol. 67, No. 11, 2487–2491, Nov. 2020.

[7] Li, W. T., H. R. Zhang, X. J. Chai, Y. Q. Hei, J. C. Mou, and X. W. Shi, "Compact dual-band balanced-to-unbalanced filtering power divider design with extended common-mode suppression bandwidth," *IEEE Microwave and Wireless Components Letters*, Vol. 32, No. 6, 511–514, Jun. 2022.

[8] Gomez-Garcia, R., M. Sanchez-Renedo, B. Jarry, J. Lintignat, and B. Barelaud, "A class of microwave transversal signal-interference dual-passband planar filters," *IEEE Microwave and Wireless Components Letters*, Vol. 19, No. 3, 158–160, Mar. 2009.

[9] Wang, Y., C. Zhou, K. Zhou, and W. Wu, "Compact dual-band filtering power divider based on SIW triangular cavities," *Electronics Letters*, Vol. 54, No. 18, 1072–1074, Sep. 2018.

[10] Ravelo, B. and O. Maurice, "Kron-Branin modeling of YY-tree interconnects for the PCB signal integrity analysis," *IEEE Transactions on Electromagnetic Compatibility*, Vol. 59, No. 2, 411–419, Apr. 2017.

[11] Ravelo, B., O. Maurice, and S. Lallechere, "Asymmetrical 1 : 2 Y-tree interconnects modelling with Kron–Branin formalism," *Electronics Letters*, Vol. 52, No. 14, 1215–1216, Jul. 2016.

[12] Ravelo, B., "Tee power divider and combiner based negative group delay topology," *International Journal of RF and Microwave Computer-Aided Engineering*, Vol. 28, No. 9, 1–9, Nov. 2018.

[13] Liu, Y., L. Zhu, and S. Sun, "Proposal and design of a power divider with wideband power division and port-to-port isolation: A new topology," *IEEE Transactions on Microwave Theory and Techniques*, Vol. 68, No. 4, 1431–1438, Apr. 2020.

[14] Wei, F., X.-B. Zhao, and X. W. Shi, "A balanced filtering quasi-yagi antenna with low cross-polarization levels and high common-mode suppression," *IEEE Access*, Vol. 7, 100 113–100 119, Jul. 2019.